

pubs.acs.org/JACS Article

High Entropy Protected Sharp Magnetic Transitions in Highly Disordered Spinel Ferrites

Lujin Min, John P. Barber, Yu Wang, Sai Venkata Gayathri Ayyagari, Gabriela E. Niculescu, Evan Krysko, Gerald R. Bejger, Leixin Miao, Seng Huat Lee, Qiang Zhang, Nasim Alem, Christina M. Rost, and Zhiqiang Mao*



Cite This: J. Am. Chem. Soc. 2024, 146, 24320-24329



ACCESS

Metrics & More

Article Recommendations

Supporting Information

Supporting Information

ABSTRACT: How disorder affects magnetic ordering is always an intriguing question, and it becomes even more interesting in the recently rising high entropy oxides due to the extremely high disorder density. However, due to the lack of high-quality single crystal samples, the strong compositional disorder effect on magnetic transition has not been deeply investigated. In this work, we have successfully synthesized high-quality single crystalline high entropy spinel ferrites (Mg_{0.2}Mn_{0.2}Fe_{0.2}Co_{0.2}Ni_{0.2})_xFe_{3.x}O₄. Our findings from high-temperature magnetization and neutron diffraction experiments showed ferrimagnetic transitions at 748, 694, and 674 K for x values of 1, 1.5, and 1.8, respectively. Notably, the magnetic transition almost showed no broadening for x values of 1 and 1.5, compared to Fe₃O₄. Extended X-ray absorption fine structure measurements provided insights into the elemental distribution among the octahedral and tetrahedral sites. The random distribution of elements across these sites reduced the formation of local clusters and short-range orders, enhancing sample homogeneity and preserving the sharpness of the magnetic transition, despite bond length variation. Our study not only marks the first successful synthesis of an HEO bulk single crystal exhibiting long-range magnetic order but also sheds light on the interaction between high configurational entropy and magnetic orderings. This opens new avenues for future research and applications of magnetic high entropy oxides.

1. INTRODUCTION

The emerging "high entropy" strategy is a transformative approach to designing functional oxide materials. ^{1–5} This approach involves integrating five or more elements, of equiatomic or near-equiatomic ratios, into the cation sublattices of oxides. ² This results in extraordinary material properties that are different from those seen in conventional oxides because of the increases in chemical complexity and disorder density. A broad spectrum of the functionalities of high entropy oxides (HEOs) has been explored recently, encompassing their mechanical, ⁶ thermal, ⁷ catalytic, ^{8,9} optical, ¹⁰ and magnetic characteristics. ¹¹ Among these, the magnetic property is particularly interesting, as the high entropy tuning not only induces significant structural distortions but also simultaneously introduces extensive spin disorders by mixing different magnetic and nonmagnetic

elements. Previous research on conventional single-element-doped systems has indicated that disorders in the magnetic system can disrupt the long-range magnetic order and lead to a spin glass state, ^{12,13} or cause a broadening of the magnetic transition as a function of temperature as a result of sample nonuniformity ^{14,15} or Griffiths effect. ¹⁶ Thus, an intriguing question naturally emerges: how do the increased spin disorders and more severe lattice distortions in HEOs impact these two phenomena?

Received: April 7, 2024 Revised: August 2, 2024 Accepted: August 5, 2024 Published: August 20, 2024





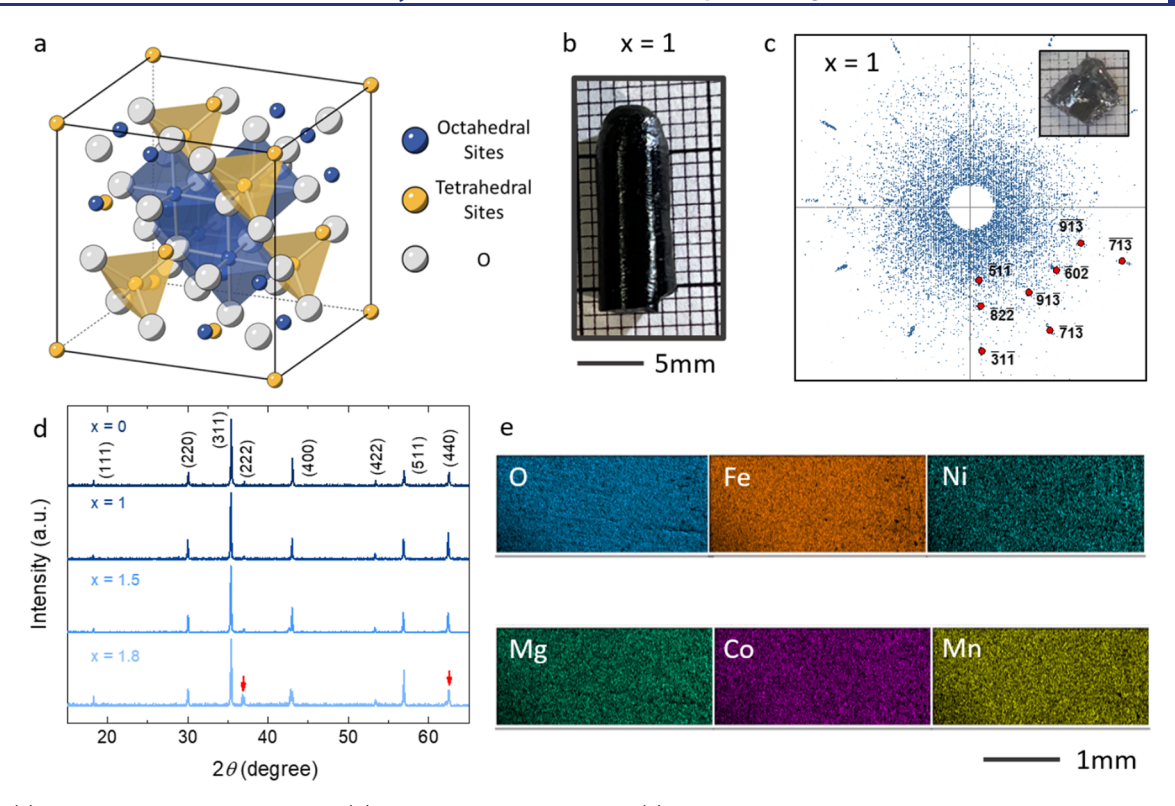


Figure 1. (a) Crystal structure of spinel oxide. (b) Crystal image of sample S1. (c) Laue pattern measured with a broken S1 piece. Inset: the shining crystal surface of the broken piece. (d) XRD pattern of S0, S1, S1.5, and S1.8, respectively. (e) Millimeter scale EDS mapping of S1.

Several studies have investigated the existence of long-range order and the spin glass state in HEOs. For instance, following the discovery of the HEO prototype, rock salt $(Mg_{0.2}Co_{0.2}Ni_{0.2}Cu_{0.2}Zn_{0.2})O$, neutron powder diffraction proved that this material possesses a long-range antiferromagnetic order below a Neel temperature (T_N) of approximately 113 K.¹¹ It was also revealed that such long-range AFM states can be tuned into spin glass states via substitutions of nonmagnetic elements. 17 According to all of these studies, generally, if the magnetic elements are not overly diluted and the magnetic frustration is not strong, the long-range magnetic order can be preserved despite extreme chemical and spin disorder, which answers the first part of the question. However, confirming changes in temperature-dependent magnetic transition is more challenging due to the lack of high-quality bulk single crystals. Compared with bulk single crystals, polycrystalline samples tend to be more inhomogeneous, which can cause transition broadening, even without high entropy tuning. To date, there are only three reported single crystals of HEOs, including rare-earth pyrochlore, 18 aluminate garnet, 19 and aluminate spinel. 20 Unfortunately, these materials do not show long-range magnetic orders but instead possess spin glass ground states. Therefore, they are not ideal candidates for investigating the impact of high entropy on magnetic transitions.

Spinel high entropy oxide (S-HEO) with the general formula $A^{2+}B_2^{3+}O_4$ is recognized as a suitable candidate for studying the magnetic properties, as well as the structural-magnetic interplay of HEOs. Different from the prototype rock salt HEO, it harbors two sets of cation sublattices, each filling the octahedral and tetrahedral positions within the oxygen lattice, as shown in Figure 1a. Based on where the A^{2+} cations reside, S-HEOs can be further segmented into normal spinel and inverted spinel types. The abundant possible combinations of

A and B elements make S-HEO capable of presenting various magnetic states, including paramagnetism, ²² ferrimagnetism, ²³ antiferromagnetism,²³ and spin glass²³ states. High entropy engineering makes such materials even more complex and flexible and, thus, more interesting. Among the S-HEOs, a particular compound that has been extensively researched is $(Co_{0.2}Cr_{0.2}Fe_{0.2}Mn_{0.2}Ni_{0.2})_3O_4$ which is designed based on the well-known ferrimagnet Fe_3O_4 . Similar to its parent compound, $(Co_{0.2}Cr_{0.2}Fe_{0.2}Mn_{0.2}Ni_{0.2})_3O_4$ is also a roomtemperature ferrimagnet with a curie temperature of about 676 K.²⁵ Comprehensive investigations have revealed its nonuniform element distribution across two cation sublattices, and subsequent experiments have manifested that Ga substitution can significantly alter the element distribution and modify its magnetic properties. Accordingly, Fe₃O₄based S-HEO is an ideal platform to explore how entropy tuning impacts the magnetic transition due to its robust longrange ferrimagnetic orders and high tunability if high-quality single crystals can be synthesized.

In this study, we report on the structure and magnetic properties of a new series of Fe_3O_4 -based S-HEO, $(Mg_{0.2}Mn_{0.2}Fe_{0.2}Co_{0.2}Ni_{0.2})_xFe_{3-x}O_4$ with x values of 1, 1.5, and 1.8. We synthesized high-quality bulk single crystals utilizing the optical floating zone method. These crystals were subsequently verified via X-ray diffraction, Laue diffraction, and energy dispersive X-ray spectroscopy. Our findings from high-temperature magnetization and neutron diffraction experiments showed ferrimagnetic transitions at 741, 694, and 672 K for x values of 1, 1.5, and 1.8, respectively. Compared with Fe_3O_4 , there was no significant broadening observed in the temperature-dependent magnetic transition for the cases where x equals 1 and 1.5. However, a slight broadening was noticed when x equals 1.8. Extended X-ray absorption fine structure measurements were performed to gain insight on the

distribution of the elements among the octahedral and tetrahedral sites. Partial inversions of the elements were observed confirming that both sites were occupied by multiple elements. The randomly distributed multiple elements on both sites could decrease the possibility of the formation of the local clusters and short-range orders through the high entropy effect, which was confirmed by transmission electron microscopy. Thus, such a high entropy effect enhances the homogeneity of the sample, and further protects the sharpness of the magnetic transition. This study not only marks the first successful synthesis of an HEO bulk single crystal exhibiting long-range magnetic order but also sheds light on the interaction between high configurational entropy and magnetic orderings. This opens new avenues for future research and applications of magnetic high entropy oxides.

2. RESULTS

2.1. Crystal Growth and Characterization. Three high entropy spinel compounds $(Mg_{0.2}Mn_{0.2}Fe_{0.2}Co_{0.2}Ni_{0.2})_xFe_{3-x}O_4$ with x values of 1, 1.5, and 1.8 were synthesized. Together with the parent phase Fe₃O₄, we refer to them respectively as S0, S1, S1.5, and S1.8 for convenience. The starting reactants, MgO, MnO, FeO, CoO, NiO, and Fe₂O₃ powders, were first weighed and fully mixed and then transferred into a cylindrical balloon and pressed into a long rod by hydrostatic pressure. The rod was later divided into two pieces: a seed rod and a feed rod. Both rods were sintered at 1523 K for 48 h in air and then cooled down to room temperature with the furnace. Subsequently, the rods were loaded into an optical floating zone furnace for single crystal growth under a mixed atmosphere consisting of 90% Ar and 10% O₂. The growth process was carried out at a feed rate of 4 mm/h and growth speed of 4-8 mm/h, which facilitated a stable melt zone and subsequent good single crystal formation. Black crystals with approximate diameters of 5 mm were obtained, as illustrated in Figure 1b for sample S1. The growth of materials with x larger than 1.8 was not successful due to the absence of a stable melt zone. The reason is that during the floating zone growth Fe₂O₃ with a relatively low melting point functioned as a flux. When x became larger, there was less Fe₂O₃ in the mixed powder, and then raw materials with high melting points, such as MgO, MnO, CoO, and NiO, could not fully melt in the flux, thereby preventing them from fully reacting.

The quality of the resultant single crystals was evaluated by using Laue diffraction. In the case of S1 and S1.5 which formed a single-domain crystal, the breaking of large crystal rods into smaller pieces reveals shiny flat surfaces, as demonstrated in the inset of Figure 1c. These surfaces correspond to the (1 0 0) crystal plane, whose Laue diffraction pattern is shown in Figure 1c. In contrast, sample rod S1.8 consists of many submillimeter-sized tiny crystals rather than a single crystal with only one large domain. This resulted from the low Fe₃O₄ flux ratio mentioned above. Moreover, some parts of the broken crystal rods were ground into powder for conducting X-ray diffraction (XRD) measurements to check the phase purity. As shown in Figure 1d, all three high entropy samples share XRD patterns similar to those of the parent compound Fe₃O₄, meaning that these samples crystallize in the same spinel structure. Despite increasing x values, the locations of all of the diffraction peaks remain almost constant, suggesting that the lattice parameter remains unchanged across different entropy levels. It is also important to mention that the S1.8

sample reveals slight splitting on the (222) and (440) peaks as labeled in Figure 1d, indicating the nonuniformity or lattice distortion within the sample.

We also conducted composition analyses using energy dispersive spectroscopy (EDS) for all of the samples to reveal their real compositions, which are listed in Table 1. To

Table 1. Nominal and Actual Compositions of Each Synthesized Material^a

label	S0	S1	S1.5	S1.8
nominal actual	Fe_3O_4	AFe_2O_4 $A_{1.05}Fe_{1.95}O_4$	A _{1.5} Fe _{1.5} O ₄ A _{1.61} Fe _{1.39} O ₄	$A_{1.8}Fe_{1.2}O_4$ $A_{1.72}Fe_{1.28}O_4$
Mg		3.2	5.4	5.0
Mn		3.2	5.3	6.1
Co		3.0	5.8	5.8
Ni		3.0	5.5	6.2
Fe		31.9	29.4	27.4
O		55.8	48.7	49.3

^aThe Numbers Shown in the Table are in at %.

simplify, the chemical formulas are abbreviated as A_xFe_{3-x}O₄ by assuming all of the elements on the A site share similar atomic ratios. It is worth mentioning that the at% of Fe in A is estimated by the average value of at% of (Mg, Mn, Co, Ni). The EDS mapping of S1 shown in Figure 1e demonstrates the uniformity of the crystal in the submillimeter scale; the mappings of other samples are included in Supporting Information Note 1

2.2. Magnetization and Neutron Diffraction. The temperature dependencies of magnetization of all four samples, measured with a magnetic field of 1000 and 100 Oe under field-cooling (FC) histories, are presented in Figures 2a,b, respectively. For a clear comparison, the magnetization data of all of the samples are normalized against their magnetization value at 300 K, where the magnetizations of the samples are fully saturated with a 100 Oe external magnetic field. Samples S1 and S1.5 show broad peaks near 400 K under a 1000 Oe magnetic field (Figure 2a), which is attributable to changes in the magnetic domain structure and the pinning effect of domain walls. Compared with the parent compound S0 which exhibits a sharp ferrimagnetic transition at 841 K, the high entropy variants S1 and S1.5 show similar abrupt transitions at 748 and 694 K, respectively. Conversely, sample S1.8 exhibits a more gradual transition with an onset of 674 K, mostly attributed to its internal nonuniformity, as confirmed by split XRD peaks and tiny crystal domains. To quantitatively compare the sharpness of the transition, we defined the transition width as the temperature range between the onset T_c and the temperature where the magnetization reaches 20% of the magnetization of 300 K at the 100 Oe external field. As demonstrated in the inset of Figure 2b, the transition widths are 1.78 1.64, 3.1, and 5.79 K for S0, S1, S1.5, and S1.8, respectively. We noted that the transition width of S1 is even smaller than that of parent phase Fe₃O₄. This can be attributed to fluctuations in floating zone crystal growth conditions, such as small variations in melting-zone temperature and pressure in the growth chamber, which can lead to small variations in crystal defect density, even for different batches of growth with the same composition. In the inset of Figure 2b, we also plotted the transition temperature T_c as a function of x. This relationship can be fitted linearly, indicating that the magnetic interactions in all three high entropy spinels are consistent with

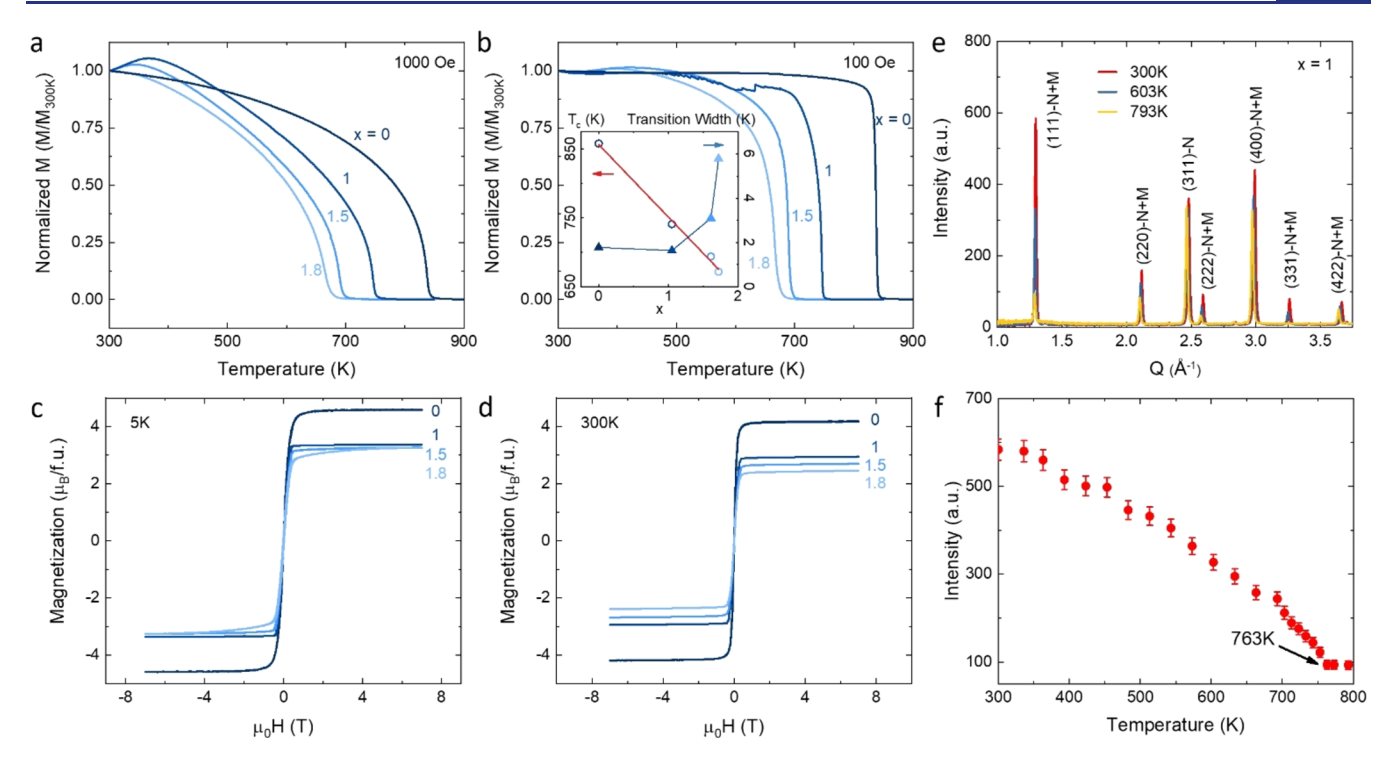


Figure 2. (a, b) Temperature-dependent magnetization of S0, S1, S1.5, and S1.8 with (a) 1000 Oe and (b) 100 Oe external magnetic field. Inset: Curie temperatures and transition widths of all four samples. (c, d) Isothermal magnetizations vs magnetic field at (c) 5 K and (d) 300 K. (e) Neutron powder diffraction patterns of S1 measured at different temperatures. (f) Temperature dependence of the (111) nuclear and magnetic peak intensity. A clear anomaly at 763 K can be observed.

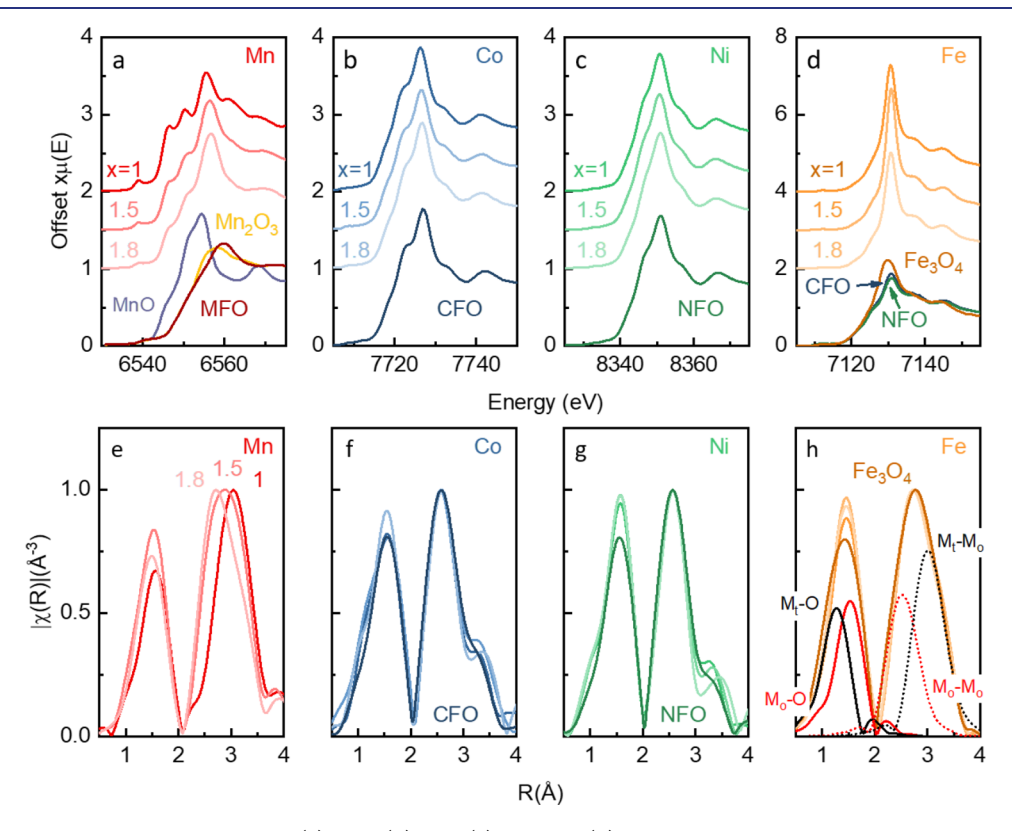


Figure 3. (a-d) Normalized XANES spectra for (a) Mn, (b) Co, (c) Ni, and (d) Fe K-edges in each spinel composition compared to both measured and literature-based references. (e-h) Absorber-specific comparison of FT EXAFS $|\chi(R)|$ for (e) Mn, (f) Co, (g) Ni, and (h) Fe absorbers in all measured samples and standards. Data are normalized to the largest peak for simplified viewing. MFO, CFO, and NFO represent MnFe₂O₄, CoFe₂O₄, and NiFe₂O₄, respectively.

those in the parent materials (Supporting Information Note 2). This characteristic, along with the configurational homogeneity provided by high entropy, plays a critical role in maintaining the sharpness of the magnetic transition.

The isothermal magnetization measured at 5 and 300 K demonstrates all of these high entropy compounds to be soft magnets with negligible coercivity, as illustrated in Figure 2c,d. At 300 K, S1, S1.5, and S1.8 quickly saturate to 2.90, 2.65, and 2.39 $\mu_{\rm B}/{\rm f.u.}$ when the magnetic field reaches 0.5T. Given that the saturation moments are even smaller than that in Fe₃O₄, the ordered moments in tetrahedral and octahedral sites should be antiparallel to each other, i.e., forming a long-range ferrimagnetic order. This conclusion is also confirmed by the subsequent neutron diffraction result, as presented below. At 5 K, S1 and S1.5 display sharp saturation turns in isothermal magnetization, even sharper than that of the parent compound S0, implying the high degree of magnetic moment alignment and low resistance to domain wall movement within the samples. In contrast, S1.8 demonstrates a more gradual saturation curve, with its magnetization continuing to increase even above 5 T and reaching a similar magnetization level to that of S1.5 near 7 T.

Representative neutron powder diffraction patterns at different temperatures of the grinded S1 piece are shown in Figure 2e. Upon cooling, a magnetic contribution to a couple of low-Q peaks, such as (111), (220), (222), (400), (331), and (422), was observed. The temperature dependence of the (111) nuclear and magnetic peak intensities in Figure 2f identifies a magnetic transition of about 763 K, consistent with the magnetization measurements. The difference in transition temperature comes from the calibration error. Similar to the temperature-dependent magnetization data, a distinct magnetic transition instead of magnetic crossover is observed in the temperature dependence of the neutron scattering intensity at (111). All of the magnetic peaks can be indexed on the crystal unit cell, leading to a magnetic propagation vector $\mathbf{k} = (0.0,0)$. The relative intensity of the magnetic peaks is consistent with the ferrimagnetic magnetic model, akin to those observed in the parent compound $Fe_3O_4^{\ 28}$ and another inverse spinel $NiFe_2O_4^{\ 29}$ Therefore, both magnetization and neutron diffraction measurements demonstrate that high entropy engineering does not broaden the magnetic transition in these single crystalline S-HEOs, which is sharply contrasted with the traditional expectation that doping to a magnetic system would lead to a broadened magnetic transition as noted above. To understand this unusual phenomenon, we investigated the local structures present in these samples, as presented below.

2.3. Local Structure Determination with X-ray Absorption Fine Structure. We first measured the X-ray absorption fine structure (XAFS) of several elements in each sample. Figure 3a-d present the X-ray absorption near edge structure (XANES) of all measurable K-edges in comparison with standard references. For the Co, Fe, and Ni edges, the corresponding spinel ferrites Fe₃O₄, CoFe₂O₄, and NiFe₂O₄ were used alongside the samples. Mn standards were sourced from reference. XANES is categorized into three sections: pre-edge, absorption edge, and near edge fine structure. Pre-edge features indicate 1s to 3d transitions and vary based on the density of unoccupied 3d states and changes in coordination geometries. The main absorption edge embodies 1s to np states, with shifts mainly indicating oxidation state changes of the absorber. Oscillations above the edge are also

sensitive to the coordination geometry. Observing Co and Ni, as depicted in Figure 3b,c, their fine structures appear consistent across different sample compositions and align well with the CoFe₂O₄ and NiFe₂O₄ reference standards. Both these Co and Ni spinel ferrites are entirely inverted, with Co and Ni predominantly in octahedral positions. 32,33 For Fe, as presented in Figure 3d, the pattern aligns well with the CoFe₂O₄ and NiFe₂O₄ standards, suggesting that Fe³⁺ occupies both the tetrahedral and octahedral sites. This, compared to the broader features and slight shift in white line (near 7130 eV) of the Fe₃O₄ powder standard suggests slightly higher ratio of Fe³⁺/Fe²⁺ in the samples than pure magnetite. The Mn K-edge features, illustrated in Figure 3a, exhibit sharper and more intricate patterns compared with other edges. When juxtaposed with data from previous studies,³⁰ Mn seemingly retains multiple oxidation states across diverse site occupancies, which is also evidenced by our Electron Energy Loss Spectroscopy (EELS) results which will be shown later. On average, the oxidation state seems to rise with a reduction in the Fe content of each sample, as evidenced by shifts in both the edge and the MnFe₂O₄ line. It can be well understood as follows: the rising proportion of Mg²⁺ release fewer electrons compared with the substituted Fe³⁺. Consequently, this electron deficit necessitates compensation by other elements in the system.

Extended X-ray absorption fine structure (EXAFS) can help clarify the observations of the XANES spectra by providing further information about local environmental structure/partial pair distributions. Figure 3h illustrates generalized pair correlations for tetrahedral and octahedral sites in spinel. The solid brown line corresponds to phase-uncorrected Fourier transformed (FT) Fe $_3O_4$ EXAFS data with the first peak characteristic of nearest neighbor (NN) pairs and the second peak of next nearest neighbor (NNN) pairs. For spinel, the first peak contains information on both tetrahedral and octahedral metal—oxygen (M $_t$ -O and M $_o$ -O) pairs. The second peak consists primarily of metal—metal (M $_o$ -M $_o$ and M $_t$ -M $_o$) pairs for octahedral-octahedral and tetrahedral-octahedral cation pairs. Any multiple scattering paths within the radius of the base pairs are ignored for simplification.

The normalized FFT results of the EXAFS for each absorber are plotted in Figure 3e—h ($\chi(k)$ spectral data are shown in Supporting Information Note 3). We first consider the peak position and breadth for Fe as a reference point of comparison (Figure 3h). Fe has the highest concentration in each sample, and likely the highest probability of fully mixed occupancy. Peak breadth (or symmetry) and central position are related to both degree of inversion and lattice parameter of individual samples. From S0 to S1.8, the FT EXAFS data for Fe almost remain no change. Fe is consistently mixed.

Co and Ni, shown in Figure 3f,g respectively, appear to primarily occupy the octahedral sites, with a slight variation in tetrahedrally associated peaks. The relative intensity increases of the tetrahedral shoulders in the NN and NNN peak sets suggest Co to have a slightly higher occupancy in tetrahedral site than Ni. Generally, they exhibit similar peak structures in the NN region, splitting further than that of Fe. Clear shoulders can be observed at low phase-uncorrected R (1–1.3 Å) in the range of M_t -O, and sharper, more intense peaks in the M_o -O range of 1.3–2 Å. In the NNN region, the highest intensity peak corresponds to octahedral pairing M_{oct} - M_{oct} between 2–2.8 Å, with minor peaks for M_t - M_o between 3–3.5 Å. This is consistent with the XANES comparison, noting

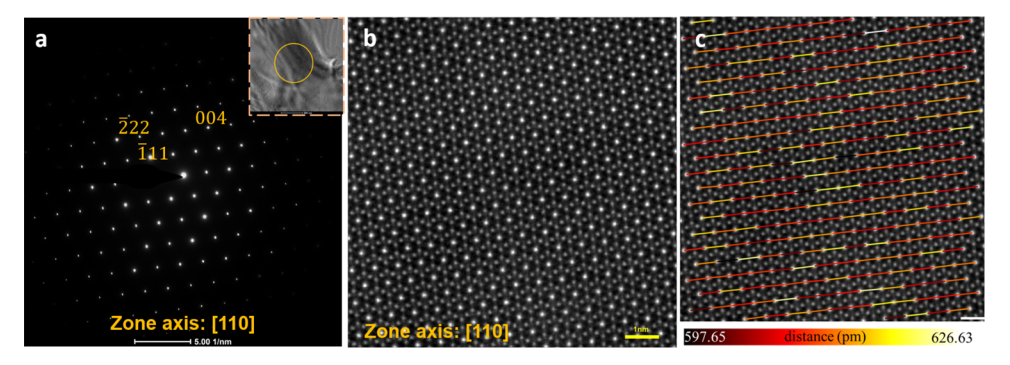


Figure 4. Investigation of structure using S/TEM: (a) Selected area electron diffraction along the [110] zone axis with inset showing the TEM image with yellow circle indicating the selected area. The scale bar is 5 nm⁻¹. (b) ADF-STEM image along the [110] zone axis confirms the formation of spinel crystal structure. Only transition metals are shown. The scale bar is 1 nm. (c) Projected interatomic distance measurements between the cations measured on STEM image (b). The colors of the lines correspond to the interatomic distances.

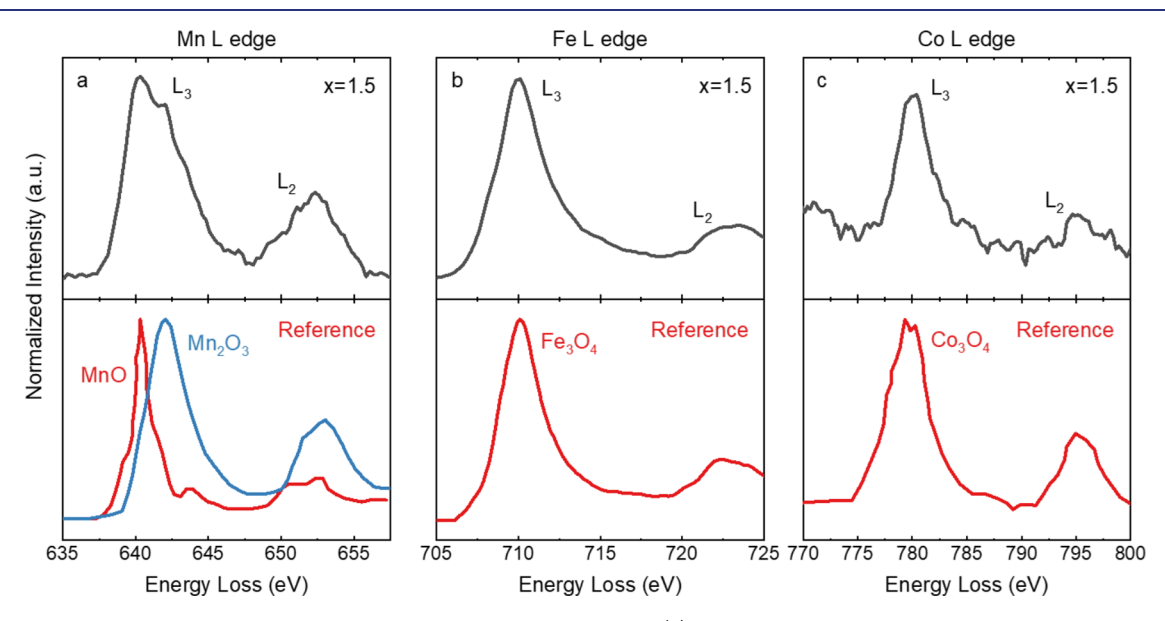


Figure 5. Investigation of oxidation states using monochromated STEM-EELS: (a) Mn L edge measured experimentally plotted with Mn EELS reference from MnO and Mn_2O_3 , confirming Mn is in both 2+ and 3+ oxidation state. (b) Fe L edge plotted with the Fe EELS reference from Fe_3O_4 showing Fe is in both 2+ and 3+ oxidation state. (c) Co L edge plotted with Co reference from Co_3O_4 , confirming Co in both 2+ and 3+ states.

that NiFe $_2$ O $_4$ and CoFe $_2$ O $_4$ parent compositions are stable in a fully inverted structure. 32,33

Finally, Mn, shown in Figure 3a, clearly shows a systematic transition in correlation from primarily tetrahedral to octahedral occupancy. For S1, a broader overall peak in the NN range expands to the NNN region, exhibiting flipped peak intensities compared to the other cations in the sample. The primary peak in this range correlated to the M_t-M_o with a minor shoulder indicating a lesser correlation between Mo-Mo. Of the cations in this composition, MnFe₂O₄ has been found to stabilize in a partially inverse site distribution^{34,35} with up to 20% inversion of Mn on octahedral sites. Thus, in the S1 composition, it seems likely that Mn primarily occupies tetrahedral sites compared with Co and Ni. When the ratio of Fe decreases, Mn exhibits a notable change in the NNN peak, which begins to broaden and shift toward Mo-Mo. This broadening, like that of the Fe peaks, suggests a larger distribution of bond lengths corresponding to multiple site occupancies compounded by the polyhedral disorder induced by multiple cation radii sharing lattice sites.

It must be noted that due to Mg's low atomic number and low X-ray absorption edge energy, direct observation of Mg distribution using EXAFS presents significant challenges. However, given the well-documented partially inverted spinel structure of MgFe₂O₄, where Mg occupies both tetrahedral and octahedral sites, ^{36,37} it is reasonable to assume that Mg in our high entropy samples is similarly distributed across both sites. Further, depending on valence and coordination, Mn has been known to exhibit Jahn—Teller characteristics that can modify fine structure, which could make the local structure more complex. ^{38,39} All of these features make the quantitative analysis complex and challenging, and such a more in-depth analysis of local structure will be detailed elsewhere.

It is also worth noting that in $(Co_{0.2}Cr_{0.2}Fe_{0.2}Mn_{0.2}Ni_{0.2})_3O_4$, Co tends to fully occupy tetrahedral sites. However, in all three samples here, Co tends to occupy more octahedral sites more. The only difference is that Mg substitutes for Cr in our samples. This phenomenon vividly demonstrates the cocktail effect in the S-HEOs.

2.4. Atomic Scale Structure Analysis via Transmission Electron Microscopy and Extended Analyses. To probe

the local structure, elemental distribution, and oxidation states of cations, Scanning/Transmission Electron Microscopy (STEM) experiments were performed on S1.5. As shown in Figure 4a, selected area electron diffraction along [110] zone axis confirms the formation of a single-phase spinel structure with no evidence of secondary phases or extra ordering in the material. The STEM imaging along [110] zone axis shown in Figure 4b is similar to what was observed in previous study on pure Fe₃O₄. Oxygen atoms are not shown due to negligible intensity compared to those of the transition metals.

Nanometer-scale EDS mapping reinforces the nonexistence of the short-range order, as shown in Supporting Information Note 4. A quantitative analysis of the structural distortion was undertaken through the calculation of interatomic distances between cations residing in octahedral sites, as depicted in Figure 4c. The observed variability in these distances, approximately 28.98 pm and accounting for a 4.7% deviation from the mean, is indicative of the inherent structural distortion brought about by the presence of multiple cation types within the lattice. The histogram of projected interatomic distances is provided in Supporting Information Note 5.

To ascertain the oxidation states of Mn, Fe, and Co ions more precisely, we performed monochromated STEM-EELS experiments. The derived L edge spectra for Mn, Fe, and Co (Figure 5a-c) suggest the coexistence of both 2+ and 3+ oxidation states within these ions, echoing the complex electronic environment present in our high entropy oxide. The observed fine structures in the EELS spectra closely match those of MnO & Mn₂O₃, ⁴¹ Fe₃O₄, ⁴² and Co₃O₄, ⁴³ reported in previous literature, offering a coherent picture with the findings from our XANES analysis shown in Figure 3.

3. DISCUSSION AND SUMMARY

From our qualitative analysis focusing on the local structure of these S-HEOs, it is evident that the lattice distortions are pronounced with both tetrahedral and octahedral sites being occupied by various elements. Previous studies have also reported that many doped spinel ferrites exhibit short-range order or cluster behaviors in their crystal and magnetic structures. 44-48 Should similar phenomena occur in our S-HEO samples, we would expect noticeable broadening in magnetic transitions. However, this did not happen to S-HEO samples (S1 and S1.5) and the magnetic transitions observed in these two samples are almost as sharp as that in Fe₃O₄ (Figure 2b). This can be considered to be the "high entropy effect" within the sublattice. In S-HEOs, while crystal field effects are dominant and lead to significant site selectivity, configurational entropy is still a critical factor. It acts as a deterrent against the formation of short-range order and cluster states, thereby maintaining a homogeneously random chemical and spin environment. In other words, the sharp magnetic transitions observed in our S-HEOs are preserved by high entropy, sharply contrasted with a traditional expectation that lattice disorders and local structure distortions would generally cause smearing of the magnetic transitions. Also, our claim should apply to other types of high entropy oxides, as exemplified in antiferromagnetic high entropy tungsten oxide A⁶WO₄⁴⁹ and high entropy rock salt oxides. ⁵⁰ This new finding challenges our conventional understanding of the effect of disorders on magnetic transitions in alloys and underscores the unique properties of high entropy systems.

It is important to clarify the definition of homogeneous in the context of this work. Given the nature of the spinel and site preferences based on crystal field stabilization, we cannot claim chemical homogeneity as a random and even distribution of specific cations across both tetrahedral and octahedral sites. The results of the FT EXAFS show trends toward site preference in multiple cations. We can, however, based on the lack of evident clustering in STEM, note that there appears to be a homogeneous distribution of cations across the long-range structure and thus is globally chemically homogeneous.

Lastly, we revisit S1.8, which has the lowest crystalline quality. In this sample, elements such as Mn, Co, and Ni all show a preference for occupying octahedral sites. This specific site occupancy suggests that the entropy at the tetrahedral sites is relatively low. As a result, the possibility of observing shortrange order or clustering effects in this sample is potentially higher compared to other S-HEO samples we've examined. While it is evident that the broadening of magnetic transition in S1.8 could primarily be attributed to its inferior sample quality, we cannot discount the possibility that the reduced entropy at tetrahedral sites may further amplify this trend.

In conclusion, through the synthesis of high-quality bulk single crystals and subsequent measurements, we have demonstrated that the introduction of high entropy into Fe₃O₄ base spinel oxide not only preserves long-range magnetic order but also mitigates the broadening of magnetic transitions commonly expected in highly disordered systems. Our findings challenge the conventional wisdom that increased disorder and lattice distortions inherently lead to the smearing of magnetic transitions, highlighting the unique role of configurational entropy in stabilizing and fine-tuning the magnetic properties in this system. Our study not only marks a significant advancement in the understanding of magnetic high entropy oxides but also opens new avenues for the design and optimization of high entropy functional materials.

4. EXPERIMENTAL SECTION/METHODS

- 4.1. Magnetization Measurement. The magnetization measurements were carried out with the oven module of a Quantum Design MPMS3 SQUID magnetometer. The warming rate for each magnetization versus temperature curve is 5 K/min.
- **4.2. Neutron Diffraction.** Neutron powder diffraction experiments were conducted at the time-of-flight neutron diffractometer POWGEN in the Spallation Neutron Source (SNS), located at Oak Ridge National Laboratory (ORNL). A vacuum MICAS furnace was adopted as the sample environment to cover the temperature region of 300-1473 K. Temperature dependence of the neutron diffraction patterns were collected using the neutron bank with the center wavelength of 0.8 Å.
- 4.3. X-ray Absorption Fine Structure. X-ray absorption fine structure was collected on beamline 10-BM, MRCAT⁵¹ at the Advanced Photon Source, Argonne National Laboratory (Argonne, IL). Measurements were taken in total fluorescence yield using an Oxford Si (111) monochromator set, detuned 50% for harmonic rejection, and a 4-element Vortex silicon drift detector (Hitachi High-Tech, Japan). Spectra were collected across four K-edges: Mn (6539 eV), Fe (7112 eV), Co (7709 eV), and Ni (8333 eV), from 200 eV below to approximately 800 eV above each edge, respectively. Spectra were truncated below the next absorption edge, resulting in a maximum k-space range of ~12-13 Å-1. Data were processed and qualitatively analyzed using the Demeter suite (Athena, Artemis, and Hephaestus).
- 4.4. Scanning/Transmission Electron Microscopy. STEM experiments were performed on an aberration-corrected Titan G2 microscope at MCL, Penn State, at a 300 kV accelerating voltage. STEM images were acquired in orthogonal scan directions, and drift correction was performed using open-source MATLAB code. St

The projected interatomic distances were calculated by first identifying the atomic positions. The atomic positions were measured with sub pixel accuracy using in-house developed Easy-STEM software in MATLAB.⁵⁴ Using the atomic positions, the interatomic distance between selected cations was measured and the projected interatomic distance was plotted. The standard deviation of the measured projected bond length data (in pm) is 5.2, with a calibration of 4.4956 pm per pixel for the analyzed STEM image. The EELS data were processed using HyperSpy software, and reference EELS spectra were obtained from the literature.

Talos F200X was utilized to acquire the selected area electron diffraction at 200 kV accelerating voltage. The sample preparation was conducted using a Helios 660 Focused Ion Beam (FIB).

ASSOCIATED CONTENT

Supporting Information

The Supporting Information is available free of charge at https://pubs.acs.org/doi/10.1021/jacs.4c04765.

> Additional experimental data including EDS mappings of more samples, isolated EXAFS data, and statistical analysis of the projected interatomic distances (PDF)

AUTHOR INFORMATION

Corresponding Authors

Christina M. Rost – Department of Physics & Astronomy, James Madison University, Harrisonburg, Virginia 22807, United States; Department of Materials Science and Engineering, Virginia Polytechnic Institute and State University, Blacksburg, Virginia 24061, United States; Email: cmrost@vt.edu

Zhiqiang Mao – Department of Physics, Pennsylvania State University, University Park, Pennsylvania 16802, United States; Department of Materials Science and Engineering and Department of Chemistry, Pennsylvania State University, University Park, Pennsylvania 16802, United States; orcid.org/0000-0002-4920-3293; Email: zim1@psu.edu

Authors

Lujin Min – Department of Physics, Pennsylvania State University, University Park, Pennsylvania 16802, United States; Department of Materials Science and Engineering, Pennsylvania State University, University Park, Pennsylvania 16802, United States; o orcid.org/0000-0003-3666-4661

John P. Barber – Department of Physics & Astronomy, James Madison University, Harrisonburg, Virginia 22807, United States; Department of Materials Science and Engineering, Virginia Polytechnic Institute and State University, Blacksburg, Virginia 24061, United States

Yu Wang – Department of Physics, Pennsylvania State University, University Park, Pennsylvania 16802, United States; 2D Crystal Consortium, Materials Research Institute, The Pennsylvania State University, University Park, Pennsylvania 16802, United States

Sai Venkata Gayathri Ayyagari - Department of Materials Science and Engineering, Pennsylvania State University, University Park, Pennsylvania 16802, United States

Gabriela E. Niculescu – Department of Physics & Astronomy, James Madison University, Harrisonburg, Virginia 22807, United States

Evan Krysko - Department of Physics, Pennsylvania State University, University Park, Pennsylvania 16802, United States

Gerald R. Bejger – Department of Physics & Astronomy, James Madison University, Harrisonburg, Virginia 22807, United States; Department of Materials Science and Engineering, Virginia Polytechnic Institute and State University, Blacksburg, Virginia 24061, United States

Leixin Miao - Department of Materials Science and Engineering, Pennsylvania State University, University Park, Pennsylvania 16802, United States; orcid.org/0000-0002-5454-5765

Seng Huat Lee – 2D Crystal Consortium, Materials Research Institute, The Pennsylvania State University, University Park, Pennsylvania 16802, United States

Qiang Zhang – Neutron Scattering Division, Oak Ridge National Laboratory, Oak Ridge, Tennessee 37830, United States; orcid.org/0000-0003-0389-7039

Nasim Alem – Department of Materials Science and Engineering, Pennsylvania State University, University Park, Pennsylvania 16802, United States; oorcid.org/0000-0003-0009-349X

Complete contact information is available at: https://pubs.acs.org/10.1021/jacs.4c04765

Author Contributions

^OL.M., J.P.B., and Y.W. contributed equally to this paper.

The authors declare no competing financial interest.

ACKNOWLEDGMENTS

L.M., J.P.B., S.V.G.A., G.E.N., E.K., G.R.B., L.Miao, N.A., C.M.R., and Z.M. acknowledge the support from NSF through the Materials Research Science and Engineering Center DMR-2011839. Z.M. also acknowledges the support from NSF under Grant No. DMR-2211327. Y.W. and S.H.L. acknowledge the support provided by the National Science Foundation through the Penn State 2D Crystal Consortium-Materials Innovation Platform (2DCC-MIP) under NSF cooperative agreement DMR-2039351. J.P.B., G.E.N., G.R.B., and C.M.R. would like to express their gratitude to Drs. Joshua Wright and Yujia Ding of Sector 10: MRCAT, at the Advanced Photon Source. MRCAT operations are supported by the Department of Energy and the MRCAT member institutions. This research used resources of the Advanced Photon Source, a US Department of Energy (DOE) Office of Science User Facility operated for the DOE Office of Science by Argonne National Laboratory under Contract No. DE-AC02-06CH11357. We also appreciate the support and resources from the Materials Characterization Lab (MCL) at Penn State.

ABBREVIATIONS

HEO, high entropy oxide; XANES, X-ray absorption near edge structure; EXAFS, extended X-ray absorption fine structure; XRD, X-ray diffraction; EDS, energy dispersive spectroscopy; FT, Fourier transform; NN, nearest neighbor; NNN, next nearest neighbor; HAADF, high-angle annular dark-field; STEM, scanning transmission electron microscopy; EELS, electron energy loss spectroscopy; SQUID, Superconducting Quantum Interference Device

REFERENCES

(1) Rost, C. M.; Sachet, E.; Borman, T.; Moballegh, A.; Dickey, E. C.; Hou, D.; Jones, J. L.; Curtarolo, S.; Maria, J.-P. Entropy-stabilized oxides. Nat. Commun. 2015, 6 (1), No. 8485.

(2) Kotsonis, G. N.; Almishal, S. S. I.; Marques dos Santos Vieira, F.; Crespi, V. H.; Dabo, I.; Rost, C. M.; Maria, J.-P. High-entropy oxides:

- Harnessing crystalline disorder for emergent functionality. J. Am. Ceram. Soc. 2023, 106 (10), 5587–5611.
- (3) Oses, C.; Toher, C.; Curtarolo, S. High-entropy ceramics. *Nat. Rev. Mater.* **2020**, *5* (4), 295–309.
- (4) Salian, A.; Mandal, S. Entropy stabilized multicomponent oxides with diverse functionality a review. *Crit. Rev. Solid State Mater. Sci.* **2022**, *47* (2), 142–193.
- (5) Musicó, B. L.; Gilbert, D.; Ward, T. Z.; Page, K.; George, E.; Yan, J.; Mandrus, D.; Keppens, V. The emergent field of high entropy oxides: Design, prospects, challenges, and opportunities for tailoring material properties. *APL Mater.* **2020**, *8* (4), No. 040912.
- (6) Hong, W.; Chen, F.; Shen, Q.; Han, Y.-H.; Fahrenholtz, W. G.; Zhang, L. Microstructural evolution and mechanical properties of (Mg,Co,Ni,Cu,Zn)O high-entropy ceramics. *J. Am. Ceram. Soc.* **2019**, 102 (4), 2228–2237.
- (7) Braun, J. L.; Rost, C. M.; Lim, M.; Giri, A.; Olson, D. H.; Kotsonis, G. N.; Stan, G.; Brenner, D. W.; Maria, J.-P.; Hopkins, P. E. Charge-Induced Disorder Controls the Thermal Conductivity of Entropy-Stabilized Oxides. *Adv. Mater.* **2018**, *30* (51), No. 1805004.
- (8) Chen, H.; Fu, J.; Zhang, P.; Peng, H.; Abney, C. W.; Jie, K.; Liu, X.; Chi, M.; Dai, S. Entropy-stabilized metal oxide solid solutions as CO oxidation catalysts with high-temperature stability. *J. Mater. Chem.* A **2018**, 6 (24), 11129–11133.
- (9) Edalati, P.; Wang, Q.; Razavi-Khosroshahi, H.; Fuji, M.; Ishihara, T.; Edalati, K. Photocatalytic hydrogen evolution on a high-entropy oxide. *J. Mater. Chem. A* **2020**, *8* (7), 3814–3821.
- (10) Kotsonis, G. N.; Meisenheimer, P. B.; Miao, L.; Roth, J.; Wang, B.; Shafer, P.; Engel-Herbert, R.; Alem, N.; Heron, J. T.; Rost, C. M.; Maria, J.-P. Property and cation valence engineering in entropy-stabilized oxide thin films. *Phys. Rev. Mater.* **2020**, *4* (10), No. 100401.
- (11) Zhang, J.; Yan, J.; Calder, S.; Zheng, Q.; McGuire, M. A.; Abernathy, D. L.; Ren, Y.; Lapidus, S. H.; Page, K.; Zheng, H.; Freeland, J. W.; Budai, J. D.; Hermann, R. P. Long-Range Antiferromagnetic Order in a Rocksalt High Entropy Oxide. *Chem. Mater.* **2019**, *31* (10), 3705–3711.
- (12) Huang, C. Y. Some experimental aspects of spin glasses: A review. J. Magn. Magn. Mater. 1985, 51 (1), 1–74.
- (13) Binder, K.; Young, A. P. Spin glasses: Experimental facts, theoretical concepts, and open questions. *Rev. Mod. Phys.* **1986**, *58* (4), 801–976.
- (14) Wang, L.; Chen, T. Y.; Chien, C. L.; Checkelsky, J. G.; Eckert, J. C.; Dahlberg, E. D.; Umemoto, K.; Wentzcovitch, R. M.; Leighton, C. Composition controlled spin polarization in Co_{1-x}Fe_xS₂: Electronic, magnetic, and thermodynamic properties. *Phys. Rev. B* **2006**, 73 (14), No. 144402
- (15) Leighton, C.; Manno, M.; Cady, A.; Freeland, J. W.; Wang, L.; Umemoto, K.; Wentzcovitch, R. M.; Chen, T. Y.; Chien, C. L.; Kuhns, P. L.; Hoch, M. J. R.; Reyes, A. P.; Moulton, W. G.; Dahlberg, E. D.; Checkelsky, J.; Eckert, J. Composition controlled spin polarization in Co_{1-x}Fe_xS₂ alloys. *J. Phys.: Condens. Matter* **2007**, *19* (31), No. 315219.
- (16) Griffiths, R. B. Nonanalytic Behavior Above the Critical Point in a Random Ising Ferromagnet. *Phys. Rev. Lett.* **1969**, 23 (1), 17–19.
- (17) Meisenheimer, P. B.; Williams, L. D.; Sung, S. H.; Gim, J.; Shafer, P.; Kotsonis, G. N.; Maria, J.-P.; Trassin, M.; Hovden, R.; Kioupakis, E.; Heron, J. T. Magnetic frustration control through tunable stereochemically driven disorder in entropy-stabilized oxides. *Phys. Rev. Mater.* **2019**, *3* (10), No. 104420.
- (18) Kinsler-Fedon, C.; Zheng, Q.; Huang, Q.; Choi, E. S.; Yan, J.; Zhou, H.; Mandrus, D.; Keppens, V. Synthesis, characterization, and single-crystal growth of a high-entropy rare-earth pyrochlore oxide. *Phys. Rev. Mater.* **2020**, *4* (10), No. 104411.
- (19) Pianassola, M.; Loveday, M.; Chakoumakos, B. C.; Koschan, M.; Melcher, C. L.; Zhuravleva, M. Crystal Growth and Elemental Homogeneity of the Multicomponent Rare-Earth Garnet $(Lu_{1/6}Y_{1/6}Ho_{1/6}Dy_{1/6}Tb_{1/6}Gd_{1/6})_3Al_5O_{12}$. Cryst. Growth Des. 2020, 20 (10), 6769–6776.
- (20) Krysko, E.; Min, L.; Wang, Y.; Zhang, N.; Barber, J. P.; Niculescu, G. E.; Wright, J. T.; Li, F.; Burrage, K.; Matsuda, M.;

- Robinson, R. A.; Zhang, Q.; Katzbaer, R.; Schaak, R.; Terrones, M.; Rost, C. M.; Mao, Z. Studies on the structure and the magnetic properties of high-entropy spinel oxide (MgMnFeCoNi)Al2O4. *APL Materials* **2023**, *11* (10), No. 101123.
- (21) Sarkar, A.; Kruk, R.; Hahn, H. Magnetic properties of high entropy oxides. *Dalton Trans.* **2021**, *50* (6), 1973–1982.
- (22) Iqbal, M. J.; Ismail, B. Electric, dielectric and magnetic characteristics of Cr³⁺, Mn³⁺ and Fe³⁺ substituted MgAl₂O₄: Effect of pH and annealing temperature. *J. Alloys Compd.* **2009**, 472 (1), 434–440.
- (23) Kalvius, G. M.; Krimmel, A.; Hartmann, O.; Litterst, F. J.; Wäppling, R.; Tsurkan, V.; Loidl, A. Magnetism of frustrated A-site spinels (Mn,Fe,Co)Al₂O₄. *Phys. B* **2009**, 404 (5), 660–662.
- (24) Sarkar, A.; Eggert, B.; Witte, R.; Lill, J.; Velasco, L.; Wang, Q.; Sonar, J.; Ollefs, K.; Bhattacharya, S. S.; Brand, R. A.; Wende, H.; de Groot, F. M. F.; Clemens, O.; Hahn, H.; Kruk, R. Comprehensive investigation of crystallographic, spin-electronic and magnetic structure of (Co0.2Cr0.2Fe0.2Mn0.2Ni0.2)3O4: Unraveling the suppression of configuration entropy in high entropy oxides. *Acta Mater.* 2022, 226, No. 117581.
- (25) Johnstone, G. H. J.; González-Rivas, M. U.; Taddei, K. M.; Sutarto, R.; Sawatzky, G. A.; Green, R. J.; Oudah, M.; Hallas, A. M. Entropy Engineering and Tunable Magnetic Order in the Spinel High-Entropy Oxide. *J. Am. Chem. Soc.* **2022**, *144* (45), 20590–20600.
- (26) Mao, A.; Xiang, H.-Z.; Zhang, Z.-G.; Kuramoto, K.; Zhang, H.; Jia, Y. A new class of spinel high-entropy oxides with controllable magnetic properties. *J. Magn. Magn. Mater.* **2020**, 497, No. 165884.
- (27) Grzesik, Z.; Smoła, G.; Miszczak, M.; Stygar, M.; Dabrowa, J.; Zajusz, M.; Świerczek, K.; Danielewski, M. Defect structure and transport properties of (Co,Cr,Fe,Mn,Ni)₃O₄ spinel-structured high entropy oxide. *J. Eur. Ceram. Soc.* **2020**, 40 (3), 835–839.
- (28) Shull, C. G.; Wollan, E. O.; Koehler, W. C. Neutron Scattering and Polarization by Ferromagnetic Materials. *Phys. Rev.* **1951**, *84* (5), 912–921.
- (29) Ugendar, K.; Samanta, S.; Rayaprol, S.; Siruguri, V.; Markandeyulu, G.; Nanda, B. R. K. Effect of frustrated exchange interactions and spin-half-impurity on the electronic structure of strongly correlated NiFe₂O₄. *Phys. Rev. B* **2017**, *96* (3), No. 035138.
- (30) Kuo, S.-L.; Lee, J.-F.; Wu, N.-L. Study on Pseudocapacitance Mechanism of Aqueous MnFe2O4 Supercapacitor. *J. Electrochem. Soc.* **2007**, *154* (1), A34.
- (31) Lytle, F. W.; Greegor, R. B.; Panson, A. J. Discussion of x-ray-absorption near-edge structure: Application to Cu in the high-*Tc* superconductors La_{1.8}Sr_{0.2}CuO₄ and YBa₂Cu₃O₇. *Phys. Rev. B* **1988**, 37 (4), 1550–1562.
- (32) Saputro, D. E.; Utari, U.; Purnama, B. Effect of bismuth substitution on magnetic properties of CoFe₂O₄ nanoparticles: Study of synthesize using coprecipitation method. *J. Phys.: Theories Applications* **2019**, 3 (1), 9–15.
- (33) Chinnasamy, C. N.; Narayanasamy, A.; Ponpandian, N.; Chattopadhyay, K.; Shinoda, K.; Jeyadevan, B.; Tohji, K.; Nakatsuka, K.; Furubayashi, T.; Nakatani, I. Mixed spinel structure in nanocrystalline NiFe₂O₄. *Phys. Rev. B* **2001**, *63* (18), No. 184108.
- (34) Hastings, J. M.; Corliss, L. M. Neutron Diffraction Study of Manganese Ferrite. *Phys. Rev.* **1956**, *104* (2), 328–331.
- (35) König, U. Note on the Mössbauer effect in MnFe₂O₄. Solid State Commun. 1971, 9 (7), 425–427.
- (36) O'Quinn, E. C.; Shamblin, J.; Perlov, B.; Ewing, R. C.; Neuefeind, J.; Feygenson, M.; Gussev, I.; Lang, M. Inversion in $Mg_{1-x}Ni_xAl_2O_4$ Spinel: New Insight into Local Structure. *J. Am. Chem. Soc.* **2017**, *139* (30), 10395–10402.
- (37) Sai Gautam, G.; Canepa, P.; Urban, A.; Bo, S.-H.; Ceder, G. Influence of Inversion on Mg Mobility and Electrochemistry in Spinels. *Chem. Mater.* **2017**, *29* (18), 7918–7930.
- (38) Shoemaker, D. P.; Li, J.; Seshadri, R. Unraveling Atomic Positions in an Oxide Spinel with Two Jahn–Teller Ions: Local Structure Investigation of CuMn₂O₄. *J. Am. Chem. Soc.* **2009**, *131* (32), 11450–11457.

- (39) Liu, W.-W.; Wang, D.; Wang, Z.; Deng, J.; Lau, W.-M.; Zhang, Y. Influence of magnetic ordering and Jahn—Teller distortion on the lithiation process of LiMn₂O₄. *Phys. Chem. Chem. Phys.* **2017**, *19* (9), 6481–6486.
- (40) McKenna, K. P.; Hofer, F.; Gilks, D.; Lazarov, V. K.; Chen, C.; Wang, Z.; Ikuhara, Y. Atomic-scale structure and properties of highly stable antiphase boundary defects in Fe3O4. *Nat. Commun.* **2014**, 5 (1), No. 5740.
- (41) Laffont, L.; Gibot, P. High resolution electron energy loss spectroscopy of manganese oxides: Application to Mn3O4 nanoparticles. *Mater. Charact.* **2010**, *61* (11), 1268–1273.
- (42) Almeida, T. P.; Kasama, T.; Muxworthy, A. R.; Williams, W.; Nagy, L.; Hansen, T. W.; Brown, P. D.; Dunin-Borkowski, R. E. Visualized effect of oxidation on magnetic recording fidelity in pseudo-single-domain magnetite particles. *Nat. Commun.* **2014**, 5 (1), No. 5154.
- (43) Ortiz Peña, N. In Situ Liquid Phase Transmission Electron Microscopy: from Electrocatalysts to Biomaterials; Université de Strasbourg, 2019.
- (44) Mamiya, H.; Terada, N.; Furubayashi, T.; Suzuki, H. S.; Kitazawa, H. Influence of random substitution on magnetocaloric effect in a spinel ferrite. *J. Magn. Magn. Mater.* **2010**, 322 (9), 1561–1564.
- (45) Dormann, J. L.; Nogues, M. Magnetic structures in substituted ferrites. J. Phys.: Condens. Matter 1990, 2 (5), 1223.
- (46) Ivanov, V. G.; Abrashev, M. V.; Iliev, M. N.; Gospodinov, M. M.; Meen, J.; Aroyo, M. I. Short-range B-site ordering in the inverse spinel ferrite NiFe₂O₄. *Phys. Rev. B* **2010**, 82 (2), No. 024104.
- (47) Yunus, S. M.; Shim, H. S.; Lee, C. H.; Asgar, M. A.; Ahmed, F. U.; Zakaria, A. K. M. Neutron diffraction studies of the diluted spinel ferrite Zn_xMg_{0.75-x}Cu_{0.25}Fe₂O₄. *J. Magn. Magn. Mater.* **2001**, 232 (3), 121–132.
- (48) Wang, X.; Musicó, B. L.; Kons, C.; Metz, P. C.; Keppens, V.; Gilbert, D. A.; Zhang, Y.; Page, K. Local cation order and ferrimagnetism in compositionally complex spinel ferrites. *APL Materials* **2022**, *10* (12), No. 121102.
- (49) Katzbaer, R. R.; Vincent, W. M.; Mao, Z.; Schaak, R. E. Synthesis and Magnetic, Optical, and Electrocatalytic Properties of High-Entropy Mixed-Metal Tungsten and Molybdenum Oxides. *Inorg. Chem.* **2023**, *62* (20), 7843–7852.
- (50) Jimenez-Segura, M. P.; Takayama, T.; Bérardan, D.; Hoser, A.; Reehuis, M.; Takagi, H.; Dragoe, N. Long-range magnetic ordering in rocksalt-type high-entropy oxides. *Appl. Phys. Lett.* **2019**, *114* (12), No. 122401.
- (51) Kropf, A. J.; Katsoudas, J.; Chattopadhyay, S.; Shibata, T.; Lang, E. A.; Zyryanov, V. N.; Ravel, B.; McIvor, K.; Kemner, K. M.; Scheckel, K. G.; Bare, S. R.; Terry, J.; Kelly, S. D.; Bunker, B. A.; Segre, C. U.; et al. The New MRCAT (Sector 10) Bending Magnet Beamline at the Advanced Photon Source. *AIP Conf. Proc.* **2010**, *1234* (1), 299–302.
- (52) Ravel, B.; Newville, M. ATHENA, ARTEMIS, HEPHAESTUS: data analysis for X-ray absorption spectroscopy using IFEFFIT. *J. Synchrotron Radiat.* **2005**, *12* (4), 537–541.
- (53) Ophus, C.; Ciston, J.; Nelson, C. T. Correcting nonlinear drift distortion of scanning probe and scanning transmission electron microscopies from image pairs with orthogonal scan directions. *Ultramicroscopy* **2016**, *162*, 1–9.
- (54) Miao, L.; Chmielewski, A.; Mukherjee, D.; Alem, N. Picometer-Precision Atomic Position Tracking through Electron Microscopy. *JoVE* **2021**, No. 173, No. e62164.